Buss, I. J., Nash, G. R., Rarity, J. G., & Cryan, M. J. (2010). Finite-difference time domain modeling of periodic and disordered surface gratings in AlInSb light emitting diodes with metallic back-reflectors. IEEE Journal of Lightwave Technology, 28(8), 1190 - 1200. 10.1109/JLT.2010.2040803

Finite-Difference Time-Domain Modeling of Periodic and Disordered Surface Gratings in AlInSb Light Emitting Diodes With Metallic Back-Reflectors

Ian J. Buss, Geoffrey R. Nash, John G. Rarity, and Martin J. Cryan, *Senior Member, IEEE*

***Abstract*—Two-dimensional finite-difference time-domain modeling is undertaken to study the optical behaviour of midinfrared AlInSb light-emitting diode devices with close metallic back reflectors. The location of the source and mirror is investigated in detail and optimised for peak emission at $\lambda_0 = 4$ μm. A periodic surface grating is added and it is found that greater than 98% of the light at a specific wavelength may be extracted for specific grating parameters, an enhancement of ∼20-fold. A novel type of grating termed disordered-periodic is then studied and is shown to have a much broader spectral response with more than 50% of the power extracted across a broad wavelength range.**

***Index Terms*—Finite-difference time-domain modeling, integrated optoelectronics, light-emitting diodes.**

I. Introduction

THE optical extraction efficiency of conventional light-emitting diodes is fundamentally limited by the discontinuity in refractive index between the bulk dielectric in which the light is generated and the surrounding medium into which the light is emitted. In a typical semiconductor light emitting diode (LED) structure the difference in refractive index at the interface between the device and the surrounding medium $(\Delta n \sim 2.5\text{–}3)$ results in a large amount of the generated optical power being trapped within the device. This is chiefly due to total internal reflection (TIR) which imposes an approximate limit of $\sim\eta = 1/4n^2$ on the extraction efficiency of the device [1]. Moreover, for light incident within the escape cone at the dielectric interface formed by TIR further Fresnel reflection will occur. In combination these effects lead to extraction efficiencies of the order of $\sim\eta = 1/(n(n-1)^2)$ [2]. Many methods have been proposed to overcome this fundamental limitation, including adding a metallic rear reflector to the substrate side of the device [3], employing non rectangular parallelepiped chip geometries [4], [5], resonant-cavity devices [6], [7], lens immersion [8], surface patterning [9], surface roughening [10], [11], and two-dimensional surface relief diffraction gratings [12]–[15].

This study investigates the use of metallic back reflectors in conjunction with periodic and disordered surface gratings. It has long been understood that rough surfaces enable higher extraction efficiencies due to path randomisation within the bulk semiconductor. However this understanding relies on the presence of a back recycling mirror to give rays multiple escape chances at the surface. In a previous study the effect of periodic and disordered periodic surface gratings without a back mirror was examined [16]; it was found that the introduction of disorder did not automatically lead to lower extraction efficiencies, implying that a back mirror is not always necessary for increased extraction efficiency with randomised surfaces. In this study the effect of adding a back mirror is investigated together with both periodic and disordered periodic surface gratings. Although a full 3-D model was used in our previous work this study is carried out in 2-D to simplify the understanding of the effects and increase the lateral dimensions of the simulation significantly to approach the true dimensions of a LED element. This allows a larger range of grating parameters to be simulated. The reduced run-times also allow multiple realisations of disordered surfaces to be simulated from which average behaviour can be calculated. The phenomena are investigated in detail using the 2-D Finite-Difference Time-Domain (FDTD) simulation method using the freely available MEEP software package [17]. The simulations are run in parallel on a High-Performance Cluster to afford increased simulation throughput. The physical structure and parameters of the model are based on a AlInSb LED operating in the midinfrared and are described in detail in [18].

In the following section the FDTD model is described together with the process for measuring the enhancement in optical output power afforded by the mirror and the surface grating. In further sections the optimum location of the rear mirror is investigated via FDTD simulations and validated with scalar theory. The role of both perfectly periodic and disordered-periodic gratings is then investigated in detail.

II. FDTD Model

The FDTD method has been chosen to model the behaviour of the various structures [19]; it has the advantage of directly solving Maxwell's curl equations in the time-domain and as such presents a simple theoretical structure whilst allowing the

Manuscript received June 09, 2009; revised November 24, 2009. First published February 02, 2010; current version published March 31, 2010. This work was supported in part by the Engineering and Physical Sciences Research Council (EPSRC) and QinetiQ.

I. J. Buss, J. G. Rarity, and M. J. Cryan are with the Photonics Group, Department of Electrical and Electronic Engineering, University of Bristol, Bristol BS8 1UB, U.K. (e-mail: ian.buss@bristol.ac.uk; john.rarity@bristol.ac.uk; m.cryan@bristol.ac.uk).

G. R. Nash is with QinetiQ, Malvern Technology Centre, Great Malvern, Worcestershire WR14 3LG, U.K. (e-mail: grnash@qinetiq.com).

Color versions of one or more of the figures in this paper are available online at http://ieeexplore.ieee.org.

Digital Object Identifier 10.1109/JLT.2010.2040803

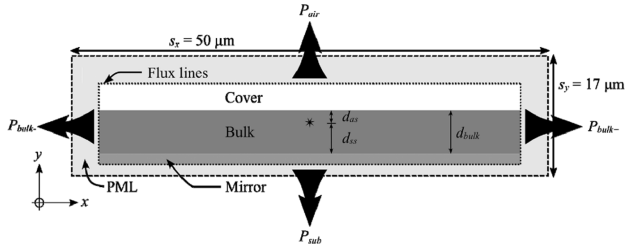

Fig. 1. Schematic illustrating the major features of the FDTD model.

broadband response of complex arbitrary geometries to be simulated. The accuracy of the model and size of domain is limited only by the available computing resources. The limitations are reduced by using parallel FDTD, which allows the computational burden to be shared by many processors. The result is reduced run-times for larger structures.

The model used in these simulations is illustrated in Fig. 1 and consists of several components, each of which may be "switched off". The simulation space is 50×17 μm in size and has three principal layers: the cover (or air) layer with $n_{\text{cover}} = 1$, the bulk layer (representing AlInSb) containing the emitting active layer with $n_{\text{bulk}} = 3.96$ and the substrate layer to represent the rear mirror. Each layer may be switched on or off with the default background refractive index being that of the bulk layer. The space is uniformly meshed with a resolution of at least $\lambda_i/15$ in all materials, where $\lambda_i = \lambda_0/n$.

A single point source, excited with a Gaussian modulated sinusoid with a centre emitting wavelength of $\lambda_0 = 4$ μm, is placed in the centre of the active layer at a distance $d_{\text{as}} = 1.03$ μm from the surface to represent an emitter in the centre of the active layer [18]. The simulation space is surrounded by perfectly matched layers (PMLs) to minimise reflections at the boundaries. In order to assess the energy flow within the simulation, virtual surfaces, or flux lines, are placed within the simulation. These monitor the total power flow out of each layer by accumulating the normal component of the Poynting vector of the Fourier-transformed fields over 50 wavelengths ranging from $\lambda_0 = 3.1$ to 5.7 μm. The vertical power flow through the flux line in the air layer, P_{air}, equates to the useful emission of the LED device through the top surface. Since, in this paper, we are not concerned with the angular distribution of the emission a far-field transformation is not performed on this data. The power flows within the bulk and substrate layers are denoted by P_{bulk} and P_{subs} respectively and the total power flow out of the simulation is given by

$$P_{\text{tot}} = P_{\text{air}} + P_{\text{sub}} + P_{bulk-} + P_{bulk+}. \tag{1}$$

The power out of each layer is normalised to the total power to ensure a sum of unity in each simulation.

III. Rear Mirror Placement

A. Scalar Theoretical Model for Back Reflector

The first step to take to improve the output power of an LED device is to place a back reflector below the emitting layer. However interference effects introduced by the formation of the cavity by the reflecting layer, the bulk material and the air surface will require careful placement of the mirror [6], [7].

Ideally, a correctly placed perfect reflector, in the absence of a cavity, can result in a four-fold increase in the output power from a single point source—or well-localised set of sources—due to the square of the superposition of direct and reflected waves. These phenomena are investigated via numerical modeling to determine the optimum placement of a rear mirror. The results are compared with a simple scalar theoretical formulation based on multiple beam summation [20]. According to this formulation, the output intensity in the external medium is given by

$$|E_{\text{ext}}|^2 = |E_{\text{in}}|^2 \times \varsigma(\psi) \times C(\phi), \tag{2}$$

where ς is the "anti-node" factor which results from the two-beam interference from the rear mirror and $C(\phi)$ is the cavity factor (a formulation of the Airy function) due to the presence of the cavity. These are defined respectively as

$$\begin{aligned} \varsigma(\psi) &= 1 + r_2^2 \pm 2r_2 \cos 2\psi \\ C(\phi) &= \frac{2T_1}{|1 - r_1 r_2 e^{-2j\phi}|^2} \end{aligned} \tag{3}$$

where $\psi = kd_{ss}\cos\theta, \phi = kL\cos\theta_i, L$ is the cavity length, d_{ss} is the location of the source from the rear mirror (see Fig. 1), θ_i is the internal angle, k is the magnitude of the wavevector $k = 2\pi n/\lambda_0, r_{1,2}$ are the Fresnel reflection coefficients at the air and mirror boundaries respectively (assuming a normal incidence), and T_1 is the power transmission at the air boundary.

The antinode factor, ζ, varies between 0 and 4 depending on the location of the source (periodic with ψ). For a single source with a metal mirror the peaks in ς occur at

$$dss = \frac{m_m \lambda_0}{4n_{\text{bulk}}}, \tag{4}$$

where m_m is any odd integer. However, this enhancement assumes a single point source, or localized set of sources such as would be found in a single quantum well. Multiple sources distributed over a larger volume, as found in a bulk or multiple quantum-well (MQW) LED, will result in a more complex result. For a bulk device the emitters are spread out over a relatively large volume (height ~ 1 μm) and so the antinode factor on the average will be somewhere between 0 and 4. As the location of a point source is varied between $d_{ss} = 0.25 - 1.25$ μm the antinode factor undergoes full range variation and has a mean value $\langle\varsigma\rangle = 1.98$. A distribution of multiple sources will then experience varying enhancement based upon their distance from the mirror. Furthermore, at larger d_{ss} the antinode factor for even a single localised emitter will experience full variation from $\varsigma = 0$–4 within the angular range of the escape cone, which will contribute to the trend of ς from its extreme values to some mean value $\langle\varsigma\rangle$. This effect is illustrated in Fig. 2 where the trend of $\langle\varsigma\rangle$ over the angular range of the escape cone is plotted for increasing d_{ss} from $\lambda_g/4$ in increments of $\lambda_g/2$, following (3). It is seen that for increasing mirror distance the role of exact mirror location becomes less and less important and the effect is tending asymptotically towards $\langle\varsigma\rangle \approx 2$. Moreover, the scalar theory is monochromatic so the effects will be different across the spectral range of emission of the LED. An optimum cavity

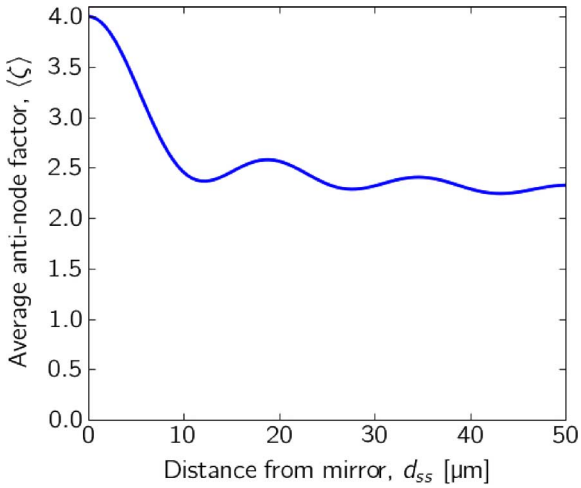

Fig. 2. Mean antinode factor for increased mirror distance.

for one wavelength will not be optimum for another. However, for clarity, in this study the LED is treated as an ideal quantum well device and a single emitter is used, with multiple sources to be treated in further studies.

It is assumed, in this case, that the unmodified internal field E_{in} emission pattern is isotropic. The presence of the cavity serves to alter the emission pattern of the source due to the influence of the cavity modes. This is illustrated in Fig. 3, where the introduction of a back reflector forms modes of emission within the cavity. Of course these patterns and effects are considered at a single wavelength. Across the full spectral emission of the LED the effects may be different and the cavity will serve to promote emission at a resonant wavelength and produce sharper spectral emission. Although not studied in this paper it must be noted that a change in the internal emission pattern may translate into an alteration in the far-field radiation pattern, deviating from the Lambertian emitter of Fig. 3(a). The cavity factor, C, is periodic with ϕ and its peaks occur with a metal mirror $(r_2 = -1)$ at cavity lengths of

$$L = \frac{m_c \lambda_0}{4 n_{\text{bulk}}}, \tag{5}$$

where m_c is any odd integer number. The spacing between optimum cavity lengths is in terms of the internal wavelength λ_i then

$$\Delta L = \lambda_0 / 2 n_{\text{bulk}} = \lambda_i / 2. \tag{6}$$

An approximate measure of extraction efficiency at a certain L and d_{ss} is then to determine the normalised proportion of $\varsigma \times C$ that falls within the escape cone of the source

$$\eta_{\text{ext}} = \frac{\int_0^{\theta_c} \varsigma \times C d\theta}{\int_0^{\pi} \varsigma \times C d\theta} \tag{7}$$

where θ_c is the critical angle at the device surface. This extraction efficiency is compared with data from the numerical FDTD simulations described in the next section.

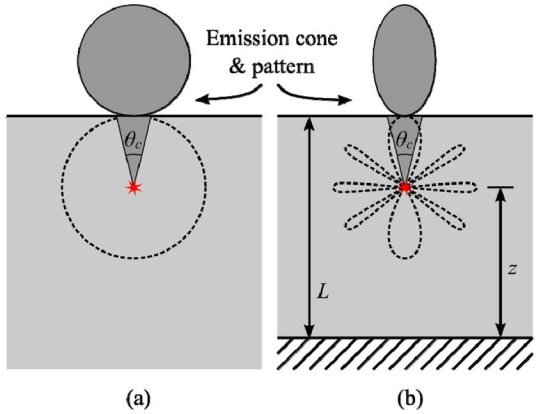

Fig. 3. Illustration of the effect of forming a cavity with a metal mirror and a dielectric surface.

B. Simulations of Metal Mirror Position

Simulations are performed for a range of source-mirror positions $d_{ss} = 0.57$–6.57 μm with $\Delta d_{ss} = 0.1$ μm with a single E_z excitation. In the model, the distance from the source to the semiconductor-air interface remains fixed at $d_{\text{as}} = 1.03$ μm to represent an emitter in the centre of the active region [18]. This distance determines whether the antinode and cavity factors vary in phase or out of phase for the wavelength under consideration. The output power will therefore be optimum for that wavelength at which the antinode and cavity factors vary in phase. The value of d_{as} should then be an integer multiple of ΔL in the case of a metal mirror. In the wavelength range of interest $d_{\text{as}} = 1.03$ μm is optimum for $\lambda_0 = 4.08$ μm.

The data for both the simulated and analytical normalised power flows are plotted in Fig. 4(a)–(c) for wavelengths of $\lambda_0 = 3.5$ μm, $\lambda_0 = 4.0$ μm and $\lambda_0 = 5.0$ μm for a range of $d_{ss} = 0 - 6.58$ μm. The data show that the simulated results follow the theory well, with the maximum normalised output intensities being seen for $\lambda_0 \approx 4.0$ μm. The results show that for a well chosen localised source-mirror position the extracted power may be > 60% of the total power at $\lambda_0 = 4.0$ μm, an enhancement of greater than fifteen-fold over a simulation without a mirror in which only 4% of the power is extracted. The optimum mirror positions for $\lambda_0 = 4.0$ μm occur at

$$d_{ss} \approx \frac{m_m \lambda_0}{4 n_{\text{bulk}}} \tag{8}$$

where m_m is any integer. (As the wavelength is close to 4.08 μm this matches (4) closely.) At this wavelength both the antinode and cavity factors are varying in phase as dss increases. The data also show that a close mirror is desirable—as d_{ss} increases the peak output power decreases. This is due to the presence of both maxima and minima (4 and 0) in the antinode factor across the angular range within the escape cone. Also the larger the cavity, the more modes it will support and less energy will appear within the escape cone. For a single source at $\lambda_0 = 4.0$ μm, or well localised set of sources, a metal mirror should therefore lie at a small as possible integer multiple of a quarter wavelength from the source.

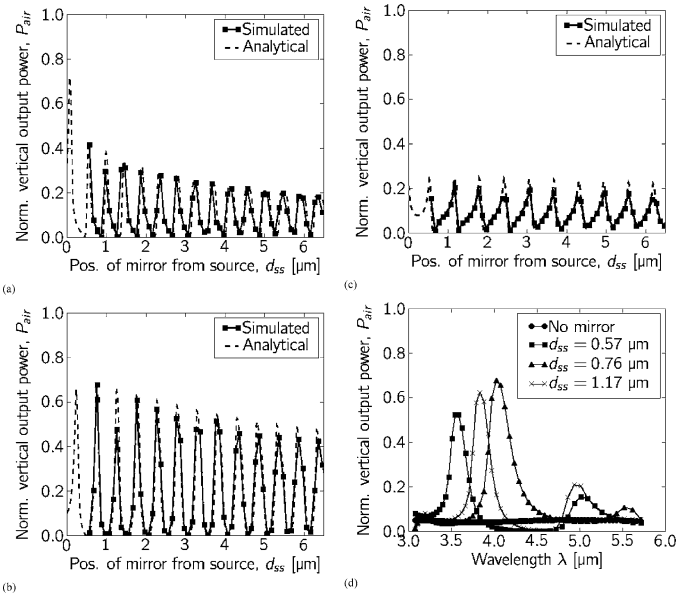

Fig. 4. Normalised output power through surface P_{air} for differing positions of a rear perfect metal reflector: (a) at $\lambda_0 = 3.5\ \mu$m; (b) at $\lambda_0 = 4.0\ \mu$m; (c) at $\lambda_0 = 5.0\ \mu$m. (d) Normalised spectral power for a flat surface and mirrors at $d_{ss} = 0.57\ \mu$m, $d = 0.76\ \mu$m and $d = 1.17\ \mu$m.

The data for $\lambda_0 = 3.5\ \mu$m and $\lambda_0 = 5.0\ \mu$m also show periodic variation. However, the magnitudes of the normalised peak intensities are not as large. This is due to the antinode and cavity factors varying with a non-zero phase difference; the fixed das is not optimal for these wavelengths. As both factors have the same periodicity the variation continues to have a period of $\lambda_i/2$. To illustrate this point further four spectral responses are plotted in Fig. 4(d) where peak values of d_{ss} for the three wavelengths are chosen together with the response for a simulation with no mirror and thus no cavity. The data show that the largest peak occurs for a wavelength of $\lambda_0 = 4.08\ \mu$m which matches the expected value from the fixed $d_{\text{as}} = 1.03\ \mu$m. The responses show the wavelength selectivity of the cavities with a large peak in output intensity at some wavelengths and a reduction in output at others. Using the normalised output intensity data, mirror positions of $d_{ss} = 0.76$, 1.77 and 2.07 μm are chosen to be simulated to investigate the responses with a grating at both peak and trough positions for output at $\lambda_0 = 4.0\ \mu$m.

C. Distributed Sources

As alluded to above, the response in the presence of a distributed set of sources will move away from the ideal case of a single source. Two simulations for two metal mirror positions, which provide both peak and trough responses at $\lambda_0 = 4.0\ \mu$m for a single source, are executed to illustrate the effect of multiple sources. The mirror positions are $d_{ss} = 1.77\ \mu$m and $d_{ss} = 2.07\ \mu$m, which give $P_{\text{air}} = 0.601$ and $P_{\text{air}} = 0.007$ respectively (see Fig. 4(a)). These same simulations are performed 100 times for different realisations of 1000 multiple sources. Each source has a uniformly random location in the notional active region ($50 \times 1\ \mu$m) and also a uniformly random start time and phase. It is found that for $d_{ss} = 1.77\ \mu$m the normalised output power becomes $P_{\text{air}} = 0.377$ and for $d_{ss} = 2.07\ \mu$m, $P_{\text{air}} = 0.043$. The multiple sources reduce the extreme variation due to the cavity, but they do not destroy it in these two cases. For the optimum output case the multiple sources reduce the peak output by 37%, while for the worst output case the output power is increased by a factor of 6. However, there is still a significant difference in output between the two cases due to the retention of the cavity factor. Thus, it is found that the mirror position remains important in spite of a diffuse set of sources, but much of the variation is reduced.

IV. Regular Surface Grating

The presence of a surface grating goes some way to overcoming the total internal reflection problem that is present when extracting light from a medium of high refractive index into a medium of low refractive index [12], [15]. This is achieved by coupling energy that is trapped in the guided modes of the high index layer into radiation modes of the air layer. The analysis of regular surface gratings may be treated with methods such as rigorous coupled wave theory, coupled mode theory [21], effective source current or volume current methods [22], [23]. In this paper we use the FDTD method to analyse these structures; the method is equally applicable for the case of regular surface gratings as for arbitrarily disordered gratings.

As outlined in a previous study [16], by using the theoretical approach outlined in [23], [24] we may estimate the grating periods which may result in enhanced output power by solving for the transmission condition at the dielectric boundary. At a smooth dielectric boundary between two media with refractive indexes n_1 and n_2 conservation of momentum requires that the tangential components of the incident and transmitted wavevectors are equal: $k_{||1} = k_{||2}$, where $k_{||1,2} = k_0 n_{1,2} \sin\theta_{1,2}, k_0 = 2\pi/\lambda_0$ and θ_1 and θ_2 are the incident and transmitted wave angles. This leads to Snell's law and a condition for transmission for an air interface

$$|k_0 n_1 \sin\theta_1| \leq k_0. \tag{9}$$

On the introduction of a surface grating an additional set of scattered tangential wavevectors, Q, is generated which serve to enable super-critical angular transmission and alter the transmission condition (9) to

$$|k_0 n_1 \sin\theta_1 - Q| \leq k_0 \tag{10}$$

The set of scattered wavevectors are defined as: $Q = Nk_q = N2\pi/\Lambda$. Unfortunately, the equations tell us nothing about the relative magnitude of these scattered waves only the range of incident angles and periods for which their wavevectors satisfy (10).

By adding the rear metal mirror strong waveguiding will occur in the bulk layer. It is clear from the results in the previous section that a rear mirror position can be chosen for a particular wavelength such that either nearly all of the light is trapped within the bulk layer as guided modes, or most of the light escapes and less is trapped. These correspond to the zeros and peaks in Fig. 4(a)–(c). It is to be expected therefore that these effects will provide further constraint on the grating parameters that give enhanced transmission through the surface and a more complex behaviour will be observed. By using a simple 'bouncing ray' approach [25] the number of modes together

TABLE I
RANGE OF GRATING PERIODS SATISFYING THE TRANSMISSION CONDITION OF (10) FOR GRATING ORDER $N = 1$ FOR THE THREE GUIDED MODES AT $\Lambda_0 = 4\ \mu$M AND $D_{\mathrm{BULK}} = 1.79\ \mu$M

Mode	Mode Angle, α	Effective Mode Index, n_{eff}	Range of Grating Periods, Λ
TE_0	74.9°	3.82	$0.21\lambda_0 \le \Lambda \le 0.37\lambda_0$
TE_1	59.0°	3.39	$0.26\lambda_0 \le \Lambda \le 0.52\lambda_0$
TE_2	40.1°	2.55	$0.38\lambda_0 \le \Lambda \le 1.56\lambda_0$

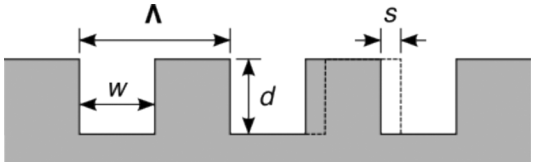

Fig. 5. Grating parameters: period Λ, width w, depth d, and random offset s.

with their bouncing angle relative to the surface normal, α, and effective index, n_{eff}, may be calculated by solving the guided mode guidance condition. A perfect metal mirror introduces a constant phase shift $\phi_m = \pi$ while the bulk-air interface introduces a variable phase shift upon total internal reflection of $\phi_{12} = 0 - \pi$. For example, at $\lambda_0 = 4\ \mu$m for a bulk layer thickness of $d_{\mathrm{bulk}} = d_{\mathrm{as}} + d_{ss} = 1.79\ \mu$m there are 3 guided modes (Transverse Electric (TE)) which may propagate in the guiding layer, each of which may be scattered by its own range of grating wavevectors Nk_q and grating periods Λ (see Table I).

A. Simulation Results

1) Surface Grating Alone: In previous work both perfectly periodic and disordered periodic gratings were studied with 3-D numerical simulations. It was found that an approximately three-fold enhancement is seen for surface features roughly on a scale with the internal wavelength $(\lambda_0/n_{\mathrm{bulk}})$ under consideration [16]. In this section these simulations are repeated in 2-D to allow a larger throughput in simulations and allow the phenomena to be investigated in greater detail at different wavelengths and in comparison to simulations with a rear reflector. In these simulations a periodic surface grating is simulated for a range of parameters (illustrated in Fig. 5) both with and without a metallic reflector. A perfectly periodic grating is initially considered with a fill factor (defined as the ratio w/Λ) $f = 0.5$ for the ranges $d = 0 - 0.9\ \mu$m and $\Lambda = 0 - 4.0\ \mu$m, with a step resolution of $\Delta d = \Delta\Lambda = 0.05\ \mu$m. As with the initial simulations a single E_z excitation is placed $d_{\mathrm{as}} = 1.03\ \mu$m from the surface.

The normalised vertical output power through the surface, P_{air}, at $\lambda_0 = 3.5\ \mu$m, $\lambda_0 = 4.0\ \mu$m and $\lambda_0 = 5.0\ \mu$m are plotted in Fig. 6(a)–(c) for a surface grating without a rear mirror. The data show that the presence of the grating enhances the output intensity at certain values of grating depth and period. The output response is highly dependent on the grating period with both enhanced and attenuated emission as compared to a flat surface as the grating serves to either promote or inhibit coupling of energy to radiation modes. Maximum output intensities of $P_{\mathrm{air}} = 0.30, P_{\mathrm{air}} = 0.24$ and $P_{\mathrm{air}} = 0.47$ are seen for $\lambda_0 = 3.5\ \mu$m, $\lambda_0 = 4.0\ \mu$m and $\lambda_0 = 5.0\ \mu$m respectively, which represent enhancements over a flat surface of 7.1, 6.0 and 9.4 respectively. The role of increased grating depth is to enhance the effect of the grating at a particular period and it plays a "coupling efficiency" role (although a more slowly varying periodicity may also be seen with depth). For larger periods a smaller depth is required to obtain an approximately equivalent effect as that seen at a smaller period. The dominant grating parameter in terms of output is then the period Λ for wavelength-scale periods.

The onset of grating effects is dependent on the wavelength under consideration and is determined from the theory to be $\Lambda \approx \lambda_0/5$. At $\lambda_0 = 3.5\ \mu$m some increases in output power which are dependent on period are seen from $\Lambda > 0.5\ \mu$m but the effects begin in earnest around $\Lambda > 0.7\ \mu$m as predicted by the theory. At $\lambda_0 = 4.0\ \mu$m and $\lambda_0 = 5.0\ \mu$m the effects begin at approximately $\Lambda > 0.85\ \mu$m and $\Lambda > 1.1\ \mu$m with some scattering seen at smaller periods. Above $\Lambda > 1.0\ \mu$m, the qualitative response from the grating is similar at all wavelengths with peaks in output seen at the same grating period intervals. These areas offer enhancement at all three wavelengths which from (10) implies that enhancement is seen for either a changing incident angle (θ_1) and constant output angle (θ_2) or constant incident angle and changing output angle. However the grating period band that exhibits the peak power varies from wavelength to wavelength. For example at $\lambda_0 = 3.5\ \mu$m the peak enhancement is seen at the $\Lambda = 2.8$–$3.0\ \mu$m band, while at $\lambda_0 = 5.0\ \mu$m the band showing peak enhancement is $\Lambda = 3.25$–$3.5\ \mu$m. Further analysis of the far-field response should reveal the behaviour in terms of incident and output angles, but as stated above this work is primarily concerned with enhancements in total power out rather than the radiation pattern. It is clear that the response of the grating to a point source is non-trivial and contains effects based on incident angle, output angle, incident wavelength, grating period and grating order. Further refinements of the model to extract this information are planned.

If we examine the normalised spectral response at grating realisations that exhibit peaks in output power we may assess the wavelength selectivity of the grating in these areas. The data is plotted in Fig. 6(d) together with the data for a flat surface. The flat surface displays a uniform spectral response. At the three gratings with peak output intensities, Fig. 6(d) (i)-(iii), there is a degree of wavelength selectivity with the peaks having a full-width half-maximum (FWHM) of $\Delta\lambda > 500$ nm. In general the data show that in a device without a rear mirror, and hence no guiding layer, a grating may provide good enhancement over a flat surface with a maximum increase of $\sim \times 9$ seen at $\lambda_0 = 5.0\ \mu$m for $d = 0.9\ \mu$m and $\Lambda = 3.3\ \mu$m. However in the parameter range simulated it is still the case that a large amount (greater than 50%) of the energy will be lost downwards through the bulk layer due to total internal reflection at the surface.

2) Surface Grating With Rear Metallic Mirror: Upon the introduction of the perfect metal back mirror the role of the grating becomes more complicated and more "dynamic". Three mirror positions are simulated: $d_{ss} = 0.76$, 1.77 and 2.07 μm to represent three different points of interest on the output response of Fig. 4(b). The normalised vertical output power through the

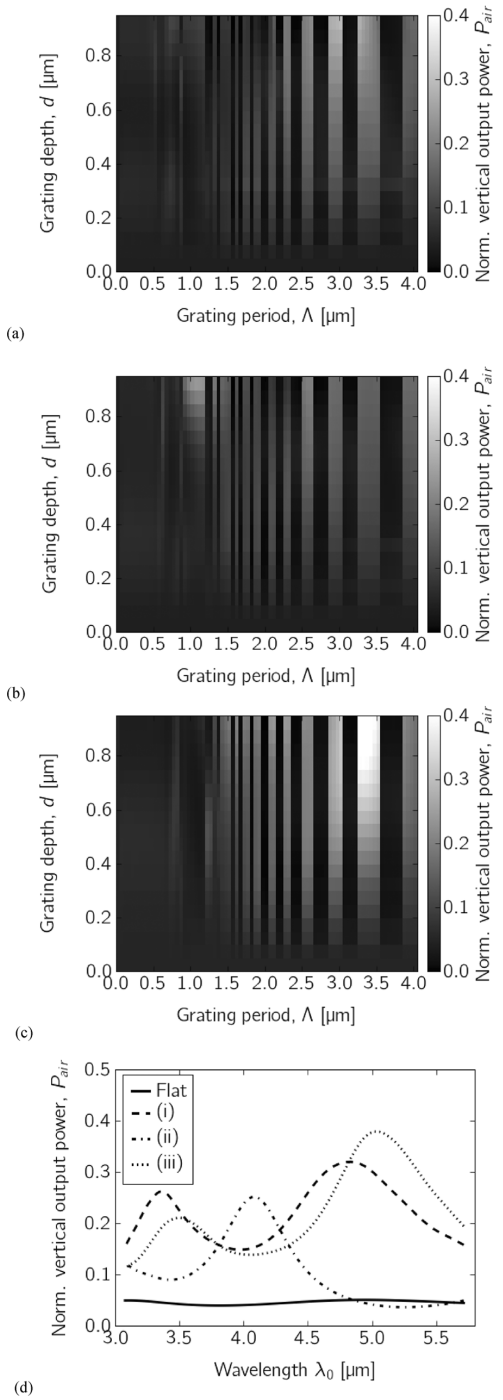

Fig. 6. Normalised output power through surface P_{air} for surface grating without rear metal reflector: (a) at $\lambda_0 = 3.5\ \mu$m; (b) at $\lambda_0 = 4.0\ \mu$m; (c) at $\lambda_0 = 5.0\ \mu$m. (d) Normalised spectral power for a flat surface and (i) $d = 0.7\ \mu$m, $\Lambda = 3.0\ \mu$m; (ii) $d = 0.9\ \mu$m, $\Lambda = 1.05\ \mu$m; (iii) $d = 0.7\ \mu$m, $\Lambda = 3.3\ \mu$m.

surface for three wavelengths $\lambda_0 = 3.5\ \mu$m, $\lambda_0 = 4.0\ \mu$m and $\lambda_0 = 5.0\ \mu$m for the three mirror locations are shown in Fig. 7(a)–(i).

The first thing to notice is that, in the parameter range simulated, there are grating configurations, which at the given wavelength, allow more than to 98% of the energy to escape through the top surface, for example at $\lambda_0 = 4.0\ \mu$m for $d = 0.6$ and $\Lambda = 2.85\ \mu$m. These optimal gratings occur at different parameters for each wavelength due to the wavelength selectivity of the grating and cavity combination. It should also be noted that these optimal grating parameters occur at both those wavelengths for which the source-mirror position is optimal for output (e.g., $\lambda_0 \approx 4.0\ \mu$m for $d_{ss} = 0.76$ or $1.77\ \mu$m) and at the wavelengths where it is non-optimal (e.g., $\lambda_0 \approx 3.5\ \mu$m at all three grating depths simulated). Thus, there are gratings that extract almost all the energy at both $\lambda_0 = 3.5\ \mu$m and $\lambda_0 = 5.0\ \mu$m for $d_{ss} = 0.76\ \mu$m, where the rear mirror and flat surface alone achieve extraction efficiencies of merely 3.5% and 4.5%; the grating enables a greater than 26-fold and 22-fold enhancement over a flat surface-mirror combination in these cases.

Two modes of grating behaviour are apparent from the data. The grating response depends on whether the source-mirror location is set for "peak output" or "peak guiding". At $\lambda_0 = 4.0\ \mu$m and $d_{ss} = 0.76$ and $1.77\ \mu$m for example (Fig. 7(d) and (e)) the behaviour displays features similar (but not identical) to that seen in the simulations without a rear mirror. In these cases the mirror position is set for maximum output power through the surface and so the guided energy is minimised; it is no surprise therefore that the behaviour shares features to simulations in which no guiding is present. However, these mirror positions do not totally eliminate guiding and so extra features are seen in which it is apparent that the guided energy is being coupled out by the grating. At $d_{ss} = 2.07\ \mu$m, where the mirror position ensures peak guiding, this "peak output" behaviour is not apparent, reinforcing the above interpretation. Instead, for "peak guiding" cases a different behaviour is seen in which peak output contours follow an upward diagonal response in several distinct lines (seen in Fig. 7(a, f, g) and i most clearly). These distinct lines correspond to the outcoupling of different modes of the system. Taking one example at $d_{ss} = 0.76\ \mu$m at $\lambda_0 = 5.0\ \mu$m (Fig. 7(g)) there are 3 calculated guided modes (see Section IV). The resultant grating period range that satisfies the transmission condition for the first mode with grating order $N = 1$ is: $1.1\ \mu\text{m} < \Lambda < 1.95\ \mu$m; and for $N = 2$ is: $2.2\ \mu\text{m} < \Lambda < 3.9\ \mu$m. These ranges delineate areas of enhancement in the grating response with the diagonal peak contours displaying the optimum parameters for the outcoupling of guided modes.

However the grating parameters which allow these optimal extraction efficiencies are in general quite narrow: for example for $d_{ss} = 0.76\ \mu$m at $\lambda_0 = 4.0\ \mu$m (Fig. 7(d)) an optimum grating occurs for a period $\Lambda = 1.45\ \mu$m and depth $d = 0.6\ \mu$m giving $P_{\text{air}} = 0.98$. A difference of ± 50 nm in the grating period means a minimum reduction in normalised output intensity of $\Delta P_{\text{air,min}} = 0.3$ (from $P_{\text{air}} = 0.98$ to 0.68 at $\Lambda = 1.5\ \mu$m) and a maximum reduction of $\Delta P_{\text{air,max}} = 0.48$ (from $P_{\text{air}} = 0.98$ to 0.50 at $\Lambda = 1.4\ \mu$m). There are, however, locations which afford more flexibility in grating parameters however: for example for deep gratings ($d > 0.8\ \mu$m) at $d_{ss} = 0.76\ \mu$m for $\lambda_0 = 5\ \mu$m and for $\Lambda \approx 2.0$–$2.2\ \mu$m and $d = 0.5$–$0.8\ \mu$m at at $d_{ss} = 0.76\ \mu$m for $\lambda_0 = 3.5\ \mu$m.

The spectral responses of some grating configurations which exhibit maxima at the chosen wavelengths are shown in Fig. 8 for the three mirror positions. They illustrate both the optimal maxima in the normalised output intensity and the wavelength selectivity of the maxima. It is immediately to be noticed that an optimum grating realisation at one wavelength may also be

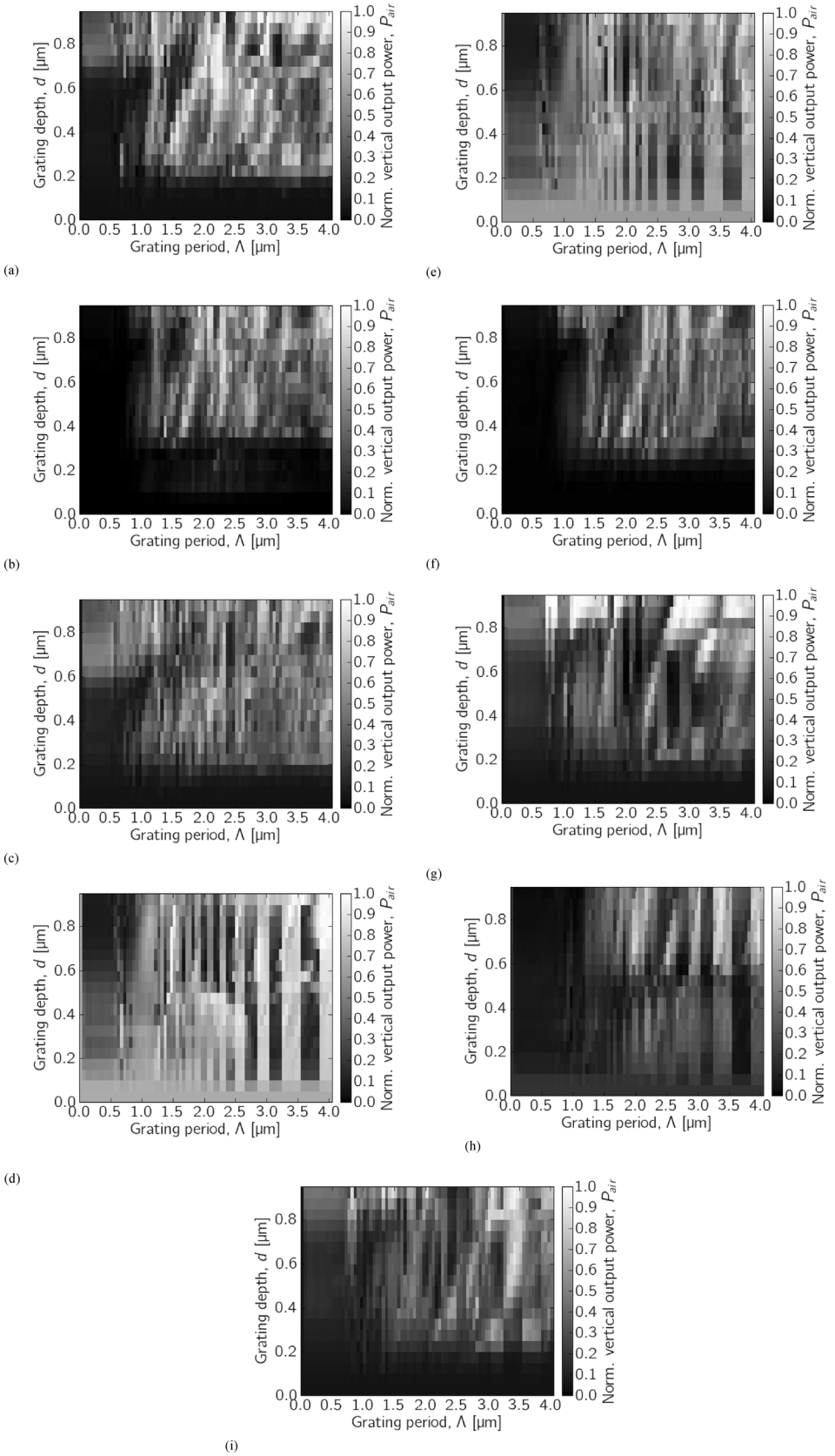

Fig. 7. Normalised vertical output power through surface P_{air} for surface grating with rear metal reflector at three wavelengths and three mirror distances: (a)–(c) at $\lambda_0 = 3.5\ \mu$m for $d_{ss} = 0.76$, 1.77 and 2.07 μm; (d)–(f) at $\lambda_0 = 4.0\ \mu$m for $d_{ss} = 0.76$, 1.77 and 2.07 μm; (g)–(i) at $\lambda_0 = 5.0\ \mu$m for $d_{ss} = 0.76$, 1.77 and 2.07 μm.

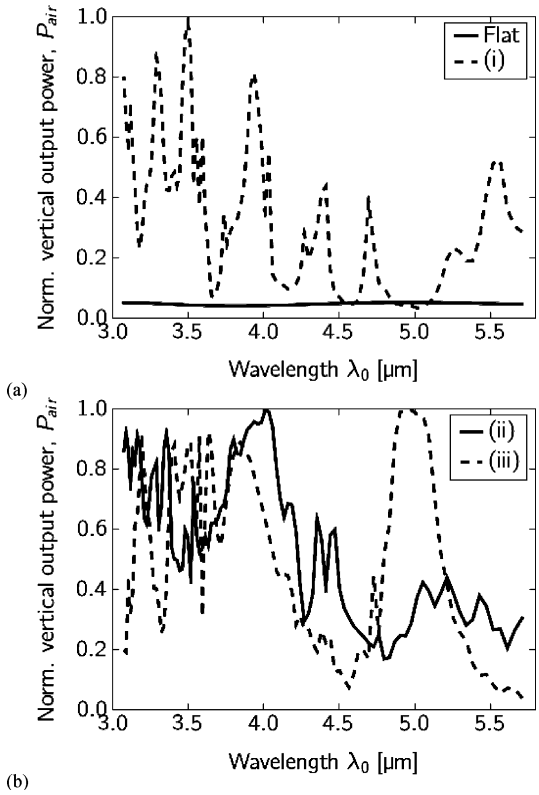

Fig. 8. Normalised spectral response of vertical output power through surface P_{air} for flat surface and optimal surface gratings with rear metal reflector at three wavelengths and $d_{ss} = 0.76\ \mu$m: (a) flat surface response and (i) optimal grating at $\lambda_0 = 3.5\ \mu$m ($\Lambda = 2.75\ \mu$m and $d = 0.55\ \mu$m); (b) optimal gratings at (ii) $\lambda_0 = 4.0\ \mu$m ($\Lambda = 2.85\ \mu$m and $d = 0.6\ \mu$m) and (iii) $\lambda_0 = 5.0\ \mu$m ($\Lambda = 1.15\ \mu$m and $d = 0.85\ \mu$m).

optimum at another but not at the wavelengths in between (e.g., at $\lambda_0 \approx 3.8\ \mu$m and $\lambda_0 \approx 5.0\ \mu$m in Fig. 8(b)(iii)). It is no surprise given that a grating at one wavelength is a higher order grating at a smaller wavelength and so on for decreasing wavelength and increasing order. The broadest simplest peak occurs around the longer wavelength of $\lambda_0 \approx 5.0\ \mu$m in Fig. 8(b)(iii); at other wavelengths the peaks are more complicated and in general less broad in wavelength. For example in Fig. 8(a)(i) the peak around $\lambda_0 \approx 3.5\ \mu$m has a full-width half-maximum (FWHM) of ~100 nm and is part of a complex spectral response, whereas in Fig. 8(b)(iii) the peak at $\lambda_0 \approx 5.0\ \mu$m has a FWHM of ~500 nm and no significant sub-peaks. This may be due to there being fewer guided modes (3 as compared to 4) at $\lambda_0 = 5.0\ \mu$m and so the grating is enhancement is clearer; the peak around $\lambda_0 = 4.0\ \mu$m (in Fig. 8(b)(ii)) is also broader but not as simple.

The spectral responses are very sensitive to wavelength because of the wavelength selectivity of both the cavity formed by the metal mirror and surface and the surface grating. The behaviour is complex and requires that the grating and mirror position be matched exactly to the desired output wavelength. However, by undertaking this optimisation it is possible, with an ideal back reflector, to extract almost all of the energy at a certain wavelength for a given emitter position.

3) Lossy Metallic Mirrors: At optical wavelengths metals become lossy and so the reflectivity deviates from the idcalised case of $\mathrm{R} = 1$ and the phase shifts on reflection $\phi \neq \pi$. The effect of lossy metals may be included in FDTD over a narrow bandwidth by equating the parameters of the frequency domain Drude model of metals with a Lorentzian harmonic representation of material polarisation in the time domain [27], [28]. Using this process a thick lossy gold mirror is placed beneath the source in place of the perfect metal. Due to the absorbing metal, the normalisation procedure used before is not appropriate as the location of the flux plane in the gold layer would not account for the losses incurred in the mirror and so the total power value would be incorrect. Instead, an enhancement factor G is defined as the ratio of the vertical output power through the top flux line to the vertical output power in a reference simulation with a flat surface and no rear mirror.

Three sets of simulations are undertaken with a lossy gold mirror with dispersive parameters determined using the method set out in Skinner *et al.* [27]. In brief, this method recognizes the similarity between the Drude model of complex permittivity in metals and the summed Lorentzian polarisabilities used in MEEP. By using readily available freuquency domain data (for example from Luxpop [29]) this may be transferred to equivalent (but narrow band) parameters for the time domain polarisability in MEEP.

The mirror is placed in three different locations from the source: $d_{ss} = 0.76$, 1.77, and 2.07 μm. The results for a surface grating with varying surface parameters are compared to those obtained for a perfect metallic mirrors. The data show that, as to be expected, the lossy mirror has a detrimental effect on the output powers seen in each case. For example, for the data at $d_{ss} = 2.07\ \mu$m, a perfect metal mirror displays an area of enhanced output of $G = 34.0$ with grating parameters of $\mathrm{d} = 0:5\ \mu$m and $\Lambda = 2.15\ \mu$m. In the lossy case, the enhancement for the same grating parameters becomes $\mathrm{G} = 22.1$, a significant fall factor 0.65. This result shows that the presence of a lossy mirror can significantly affect the output power achievable with a rear metallic mirror. As this effect will be exacerbated with increased "bounces", the mirror should be placed for peak output, or the grating designed to extract the energy with minimum "extraction length".

4) Disordered Periodic Grating: It has been observed that introducing roughness to the surface of a dielectric material, in conjunction with a rear reflecting layer, produces enhanced output powers into free space [11], [26]. In this section a periodic surface pattern, such as those investigated above, is "randomised" with varying degrees of disorder to reproduce a rough surface. An initially periodic grating composed of surface features as illustrated in Fig. 5 is disordered by applying normally distributed random offsets to each element. A single offset to a surface feature, s, is shown in Fig. 5; in ensemble the offsets have a standard deviation σ and a mean of zero. Thus, increased "randomness" is achieved by increasing the standard deviation of the offset statistics. Overlaps into neighbouring cells is allowed. It should be noted that the grating now contains an ensemble of grating periods, and consequently an ensemble of grating wavevectors [23], but due to the zero mean of the random

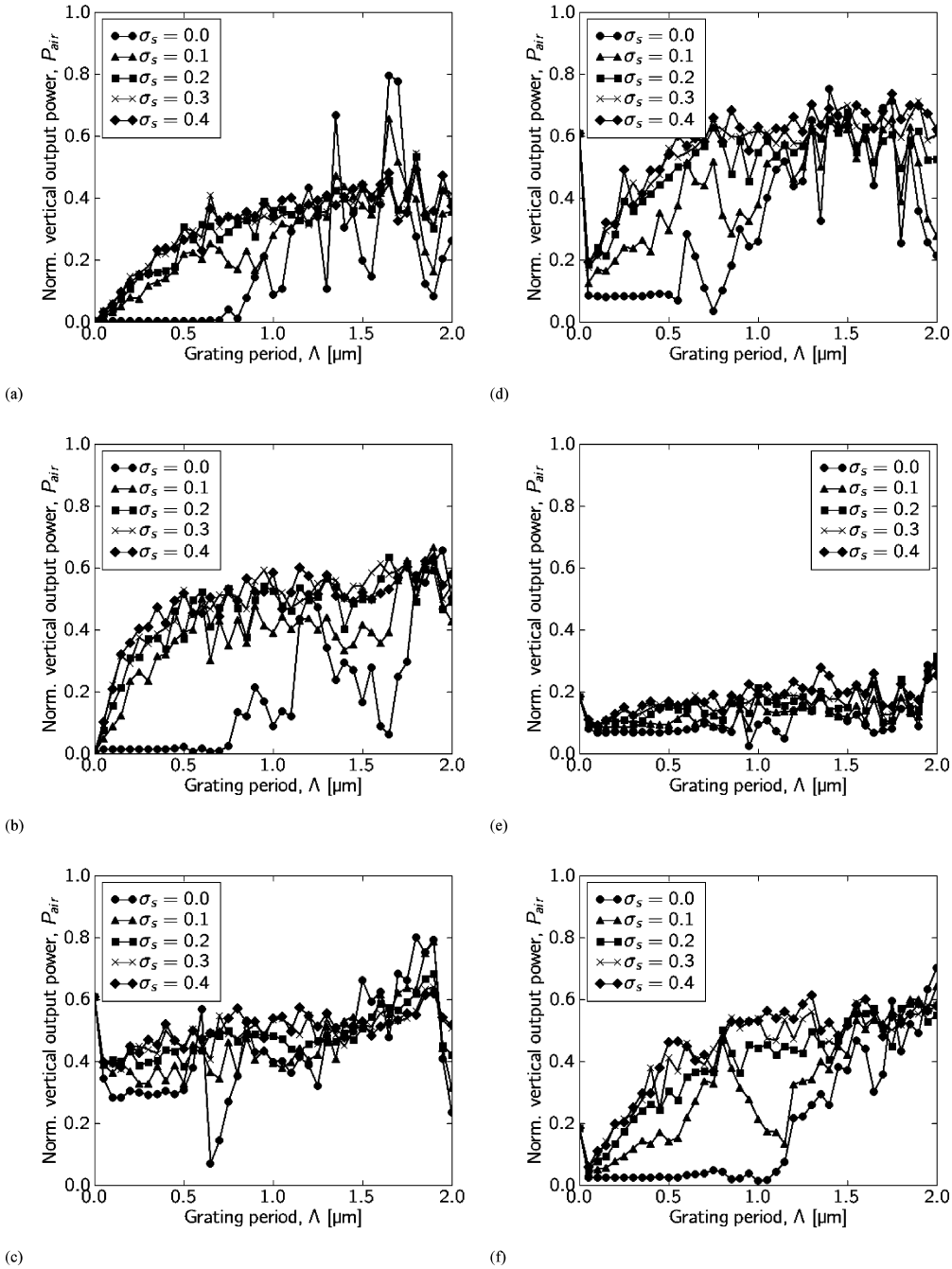

Fig. 9. Normalised output power through surface P_{air} for disordered surface gratings with rear metal reflector at two grating depths. (a)–(b) at $\lambda_0 = 3.5\ \mu$m for $d_{ss} = 0.4$, and 0.85 μm; (c)–(d) at $\lambda_0 = 4.0\ \mu$m for $d_{ss} = 0.4$, and 0.85 μm; (e)–(f) at $\lambda_0 = 5.0\ \mu$m for $d_{ss} = 0.4$, and 0.85 μm.

offsets the mean period of the grating remains that of the initial periodic grating $\langle\Lambda\rangle = \Lambda$.

Randomised gratings are investigated for a mirror position of $d_{ss} = 1.76\ \mu$m and for two grating depths $d = 0.4\ \mu$m and $d = 0.85\ \mu$m. Ten different realisations of a random grating are investigated for a given randomness σ. In order to get the general response of the randomised grating the arithmetic mean of the output powers, $\langle P_{\text{air}}\rangle$, from the ten realisations is taken. The data for random gratings from $\sigma = 0$–0.4 are shown in Fig. 9.

The data show that by adding disorder the behaviour of the surface grating is changed to become much more uniform across variations in period. Also the enhancements offered by the grating are apparent from much lower periods than for a periodic grating. The effect is most clearly seen at $\lambda_0 = 3.5\ \mu$m (Fig. 9(a) and 9(b)). The mirror position ensures that the energy is in a "peak guiding" condition as described above (cf. Fig. 9(a)) and the periodic grating $(\sigma_{\text{s}} = 0)$ does not begin to have an effect until $\Lambda = 0.7\ \mu$m (as predicted by the theory). Above this period the output power experiences large peaks and troughs dependent on the grating period. As a small amount of disorder ($\sigma_{\text{s}} = 0.1\ \mu$m) is introduced to the grating the magnitude of these variations is reduced, but they remain in large part. As the disorder is increased these variations begin

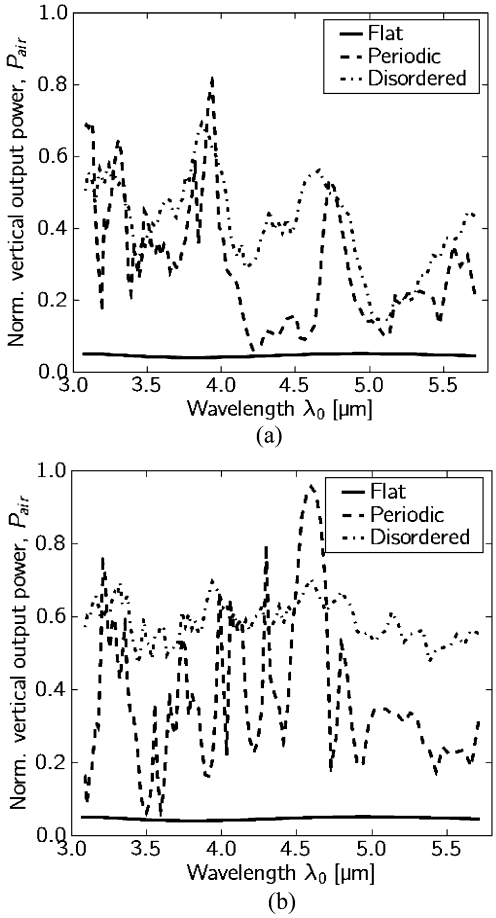

Fig. 10. Normalized spectral response of the output power through surface for simulations with (a) a flat surface, a periodic grating with $\Lambda = 1.0\ \mu$m and $d = 0.4\ \mu$m, and a disordered periodic grating with $\langle\Lambda\rangle = 1.0\ \mu$m and $d = 0.4\ \mu$m and $\sigma = 0.4\ \mu$m; (b) a flat surface, a periodic grating with $\langle\Lambda\rangle = 1.0\ \mu$m and $d = 0.85\ \mu$m and a disordered periodic grating with $\langle\Lambda\rangle = 1.0\ \mu$m and $d = 0.85\ \mu$m and $\sigma = 0.4\ \mu$m.

to disappear and the output power tends to an average value. The incident radiation, instead of experiencing a single grating period, will instead find a range of grating periods which will act to couple out a range of incident angles and wavelengths. However the strength of this outcoupling will not be as strong as if there were a perfect periodic grating and so total outcoupling as seen for the periodic grating is not seen and the total energy out will tend to somewhere between a peak and a trough for a certain wavelength (cf. Fig. 4(a)). Thus, in the limit of total randomness there is, somewhere in the pattern, always a grating period that will allow the outcoupling of radiation at a given incident angle and wavelength. In actual fact, as the standard deviation is fixed at an absolute distance the gratings with larger periods experience less "randomness" than gratings with smaller periods, which explains why some of the periodic variation re-emerges at larger periods. The role of the grating depth in its coupling efficiency role remains important as the data from $\lambda_0 = 5\ \mu$m shows (Fig. 9(e) and (f)). An increase in depth from $d = 0.4\ \mu$m to $d = 0.85\ \mu$m results in a large increase in output power.

The simulated results in Fig. 9 lead to the conclusion that a maximum normalised output power of $P_{\text{air}} > 0.5$ at all three wavelengths for a grating depth of $d = 0.85\ \mu$m is possible. By examining some spectral responses taken from these data it is possible to confirm this. Fig. 10 shows the normalised spectral response data for two grating configurations: (a) $\Lambda = 1.0\ \mu$m, $d = 0.4\ \mu$m and (b) $\Lambda = 1.6\ \mu$m, $d = 0.85\ \mu$m. For each configuration three spectral responses are shown: a flat surface reference response, a perfectly periodic grating response and a response of a disordered grating with the same mean period. The data show that at both depths the disordered response displays a considerably broader spectral response (particularly in Fig. 10b) than the perfectly periodic case and does not suffer as much from the large troughs due to the wavelength selectivity of the grating and cavity. This flatter response comes at the cost of peak power out with the disordered gratings not reaching the levels of the periodic gratings. However the data show that by tailoring the roughness it is possible to achieve a broadband spectral response which still offers considerable enhancements over a flat surface and translates the advantages afforded by the cavity to a larger wavelength range. The data also show that the disorder ought to also reduce the constraints on the source positions within the cavity as the disordered gratings show much the same response in output power at the three wavelengths considered, regardless of whether the source-mirror distance and cavity length result in a "peak output" or "peak guiding" response.

V. Conclusion

This study has investigated in detail the effects of a rear perfect back reflector, perfectly periodic surface gratings and disordered periodic surface gratings. It has been shown that a rear metal mirror in conjunction with a periodic surface grating may result in optimum extraction efficiency where more than 98% of the energy at a certain wavelength may be extracted. This behaviour is heavily dependent on specific grating parameters and mirror positions and is inherently narrowband in its spectral response. By adding disorder to the surface grating it is shown that the spectral response may be made to be much broader whilst maintaining a reasonable normalised output power ($P_{\text{air}} > 0.5$). Further investigation is underway to study these effects in more detail and refinements of the model are planned to include optical losses and real metals as well as multiple sources to represent a spontaneous emission more accurately.

References

[1] W. N. Carr, "Photometric figures of merit for semiconductor luminescent sources operating in spontaneous mode," *Infrared Phys.*, pp. 1–19, 1966.

[2] T. S. Moss, G. J. Burrell, and B. Ellis, *Semiconductor Opto-Electronics*. London: Butterworths, 1973.

[3] D. S. Wuu, S. C. Hsu, S. H. Huang, C. C. Wu, C. E. Lee, and R. H. Horng, "GaN/mirror/Si light-emitting diodes for vertical current injection by laser lift-off and wafer bonding techniques," *Jpn. J. Appl. Phys.*, vol. 43, pp. 5239–5242, 2004.

[4] M. R. Krames, M. Ochiai-Holcomb, G. E. Hofler, C. Carter-Coman, E. I. Chen, I. H. Tan, P. Grillot, N. F. Gardner, H. C. Chui, J. W. Wang, S. A. Stockman, F. A. Kish, M. G. Craford, T. S. Tan, C. P. Kocot, M. Hueschen, J. Posselt, B. Loh, G. Sasser, and D. Collins, "High-power truncated-inverted-pyramid (AlxGa1-x)(0.5)In0.5P/GaP light-emitting diodes exhibiting $>$ 50% external quantum efficiency," *Appl. Phys. Lett.*, vol. 5, pp. 2365–2367, 1999.

[5] W. Schmid, M. Scherer, C. Karnutsch, A. Plossl, W. Wegleiter, S. S. Schad, B. Neubert, and K. Streubel, "High-efficiency red and infrared light-emitting diodes using radial outcoupling taper," *IEEE J. Sel. Top. Quantum Electron.*, vol. 8, pp. 256–263, 2002.
[6] D. G. Gevaux, A. Green, C. Palmer, P. Stavrinou, C. Roberts, and C. Phillips, "Resonant-cavity light-emitting diodes (RC-LEDs) and detectors for midIR gas-sensing applications," *Proc. IEE Optoelectron.*, vol. 150, pp. 360–364, 2003.
[7] A. M. Green, D. G. Gevaux, C. Roberts, and C. C. Phillips, "Resonant-cavity-enhanced photodetectors and LEDs in the midinfrared," *Physica E*, vol. 20, pp. 531–535, 2004.
[8] J. G. Crowder, H. R. Hardaway, and C. T. Elliott, "Mid-infrared gas detection using optically immersed, room-temperature, semiconductor devices," *Meas. Sci. Technol.*, vol. 13, pp. 882–884, 2002.
[9] G. R. Nash, T. Ashley, N. T. Gordon, C. Jones, and C. Maxey, "Micromachined optical concentrators for IR negative luminescent devices," *J. Mod. Opt.*, pp. 811–820, 2002.
[10] R. Windisch, B. Dutta, M. Kuijk, A. Knobloch, S. Meinlschmidt, S. Schoberth, P. Kiesel, G. Borghs, G. Dohler, and P. Heremans, "40% efficient thin-film surface-textured light-emitting diodes by optimization of natural lithography," *IEEE Trans. Electron. Dev.*, vol. 47, pp. 1492–1498, 2000.
[11] R. Windisch, P. Heremans, B. Dutta, M. Kuijk, S. Schoberth, P. Kiesel, G. H. Dohler, and G. Borghs, "High-efficiency non-resonant cavity light-emitting diodes," *Electron. Lett.*, vol. 34, pp. 1153–1155, 1998.
[12] M. Boroditsky, T. F. Krauss, R. Coccioli, R. Vrijen, R. Bhat, and E. Yablonovitch, "Light extraction from optically pumped light-emitting diode by thin-slab photonic crystals," *Appl. Phys. Lett.*, vol. 75, pp. 1036–1038, 1999.
[13] A. David, T. Fujii, E. Matioli, R. Sharma, S. Nakamura, S. P. DenBaars, C. Weisbuch, and H. Benisty, "GaN light-emitting diodes with archimedean lattice photonic crystals," *Appl. Phys. Lett.*, vol. 88, pp. 073510–, 2006.
[14] D. Delbeke, P. Bienstman, R. Bockstaele, and R. Baets, "Rigorous electromagnetic analysis of dipole emission in periodically corrugated layers: The grating-assisted resonant-cavity light-emitting diode," *J. Opt. Soc. Am. A*, vol. 19, pp. 871–880, 2002.
[15] J. Wierer, A. David, and M. Megens, "III-nitride photonic-crystal light-emitting diodes with high extraction efficiency," *Nat. Photon.*, vol. 7, 2009.
[16] I. J. Buss *et al.*, "Three-dimensional numerical modeling of emission from InSb light-emitting diodes with patterned surfaces," *J. Opt. Soc. Amer. B*, vol. 25, pp. 810–817, 2008.
[17] A. F. Oskooi, D. Roundy, M. Ibanescu, P. Bermel, J. D. Joannopoulos, and S. G. Johnson, "MEEP: A flexible free-software package for electromagnetic simulations by the FDTD method," *Comput. Phys. Commun.*, vol. 181, pp. 687–702, 2010.
[18] M. K. Haigh, G. R. Nash, S. J. Smith, L. Buckle, M. T. Emeny, and T. Ashley, "Mid-infrared AlxIn1-xSb light-emitting diodes," *Appl. Phys. Lett.*, vol. 90, pp. 231116–, 2007.
[19] K. S. Yee, "Numerical solution of initial boundary value problems involving maxwells equations in isotropic media," *IEEE Trans. Ant. Prop.*, vol. AP-14, no. 3, pp. 302–307, May 1966.
[20] H. Benisty, H. De Neve, and C. Weisbuch, "Impact of planar microcavity effects on light extraction-Part I: Basic concepts and analytical trends," *IEEE J. Quantum Electron.*, vol. 34, no. 9, pp. 1612–1631, Sep. 1998.
[21] Y. Yamamoto, T. Kamiya, and H. Yanai, "Improved coupled mode analysis of corrugated waveguides and lasers," *IEEE J. Quantum Electron.*, vol. QE-14, no. 8, pp. 245–258, Aug. 1978.
[22] C. A. Flory, "Analysis of directional grating-coupled radiation in waveguide structures," *IEEE J. Quantum Electron.*, vol. 40, no. 7, pp. 949–957, Jul. 2004.
[23] S. Riyopoulos, "Supercritical angle transmission through quasi-random subwavelength-feature interfaces: Integral approach via effective surface currents," *J. Opt. Soc. Am. A*, vol. 22, pp. 2859–2871, 2005.
[24] S. T. Peng, T. Tamir, and H. L. Bertoni, "Theory of periodic dielect waveguides," *IEEE Trans. Microw. Theory Techniques*, vol. 23, pp. 123–133, 1975.
[25] A. Yariv and P. Yeh, *Photonics*, 6th ed. Oxford, U.K.: Oxford Univ. Press.
[26] I. Schnitzer, E. Yablonovitch, C. Caneau, T. J. Gmitter, and A. Scherer, "30% external quantum efficiency from surface textured, thin-film light-emitting diodes," *Appl. Phys. Lett.*, vol. 63, pp. 2174–2176, 1993.
[27] N. G. Skinner and D. M. Byrne, "Finite-difference time-domain analysis of frequency-selective surfaces in the midinfrared," *Appl. Opt.*, vol. 45, no. 9, pp. 1943–1950, 2006.
[28] [Online]. Available: http://ab-initio.mit.edu/wiki/index.php/Meep
[29] [Online]. Available: http://www.luxpop.com/

Ian J. Buss, photograph and biography not available at the time of publication.

Geoffrey R. Nash, photograph and biography not available at the time of publication.

John G. Rarity, photograph and biography not available at the time of publication.

Martin J. Cryan (S'91–M'95–SM'01) received the B.Eng. degree in electronic engineering from the University of Leeds, U.K., in 1986 and then worked in industry for five years as a microwave design engineer. In 1995, he received the Ph.D. degree from the University of Bath, U.K., for work on GaAs MMIC design.

From 1994 to 1997 he was a researcher at the University of Birmingham, UK where he worked on active integrated antennas. From 1997 to 1999 he was a European Union Training and Mobility of Researchers research fellow working at the University of Perugia, Italy on the design and simulation of quasi-optical multipliers using the Lumped—Element FDTD method. From 2000 to 2002 he was a research associate at the University of Bristol, UK working on hybrid electromagnetic methods for EMC problems in optical transceivers and FDTD analysis of photonic crystals. He was appointed as a lecturer in the department of Electrical and Electronic Engineering at the University of Bristol in 2002 and was made Senior Lecturer in 2007. He has published 37 journal and more than 118 conference papers (8 Invited), in the areas of fabrication, modeling and measurement of photonic crystal based devices, radio-over-fibre, active integrated antennas, FDTD analysis and MMIC design.